Identification of active sites of Pd/Al_2O_3 for CO oxidation

AUTHOR NAMES

Kazumasa Murata[†], Eleen Eleeda[†], Junya Ohyama[†, ‡], Yuta Yamamoto[§], Shigeo Arai[§] and Atsushi Satsuma[†, ‡, *]

AUTHOR ADDRESS

[†] Graduate School of Engineering, Nagoya University, Nagoya 464-8603, Japan

[‡] Elements Strategy Initiative for Catalysts and Batteries (ESICB), Kyoto University, Katsura, Kyoto 615-8520, Japan

[§] Institute of Materials and Systems for Sustainability, Nagoya University, Nagoya, Japan

KEYWORDS

Pd catalyst, CO oxidation, particle size effect, metal-support interaction, alumina, surface structure

ABSTRACT

In this work, to identify the active site of Pd/Al_2O_3 catalysts for CO oxidation, we investigated the dependence of CO oxidation activities for Pd/Al_2O_3 on surface structure and morphology of Pd nanoparticles. The maximum catalytic activity was obtained in the Pd particle size of approximately 2 nm. We performed structural analysis of Pd surface from IR spectra of adsorbed CO on Pd surface. A positive proportional relationship was obtained between catalytic activity and the fraction of linear adsorbed CO on Pd corner sites and Pd(111). Therefore, Pd corner sites and Pd(111) on Pd particle are highly active sites for CO oxidation. X-ray absorption fine structure (XAFS) and spherical aberration corrected scanning transmission electron microscopy (Cs-STEM) elucidated that < 2 nm Pd nanoparticles with amorphous-like structure and large well-ordered Pd particles are key structure to high fraction of the corner sites and Pd(111), respectively.

1. Introduction

Supported metal nanoparticle catalysts have been widely used for purification of exhaust gas from automobiles and industrial catalytic processes for chemicals. Size control of supported metal particles is effective approach to improve catalytic performance. Because the proportion of surface sites (for examples, corner and edge) on the nanoparticles changes dramatically depending on particle size.[1] For examples, the abundance of low-coordination atoms on Au clusters improve for activities of CO oxidation[2], water gas shift reaction[3,4] and aldehyde hydrogenation[5]. It has also been reported that the interfacial site between Ni, Pd and Pt

nanoparticles and CeO_2, which increases as decreasing metal particle size, promotes the CO oxidation.[6]

The crystal structure and the surface structure of metal nanoparticles, which are different from those of bulk metals, sometimes improve the catalytic performance.[7–12] Size controlling of Ru nanoparticle to 3 nm improved catalytic activity for hydrogen oxidation reaction due to generation of amorphous-like surface structure.[11] Metal-support interaction (MSI) is also one of the important factors for determining the structure of metal nanoparticles on supports.[10,13,14] Recently, we investigated that Pd particle size effect on methane combustion for Pd/Al_2O_3 with various alumina crystalline (γ- and θ-, α-Al_2O_3).[15] γ-Al_2O_3 strongly interacts with Pd species as compared with θ-Al_2O_3 and α-Al_2O_3.The morphology and surface structure of Pd particles, which were varied by Pd particle size and metal-support interaction (MSI), affected methane oxidation activity. In case of extremely low metal loadings, metal species present as an isolated metal atom on supports.[11,30] It was found that isolated metal species (such as Pt[13,20] and Pd[21], Rh[22,23], Ru[24]) is highly active as compared with nanoparticles in various catalytic reactions. It is necessary to understand the influence of their structure on catalysis for improvement of catalytic performance.

The Pd catalysts are often used as conventional catalysts for CO oxidation.[25–29] The Pd particle size effect in CO oxidation has been also discussed since about 40 years ago.[30] From a practical viewpoint of environmental purification, the importance of the catalytic activity at lower temperatures (< 200°C) is increasing. One of the keys is the effect of Pd particle size which largely changes reaction rates. Wang et al. demonstrated that the activity of CO oxidation increased with decreasing from 50–70 to 4–8 nm.[31] Osaki also reported that activity of Pd/Al_2O_3

increased as decreasing particle size in the size region of 5–14 nm.[32] Haneda et al. reported that the turnover frequency (TOF) of Pd/Al_2O_3 catalyst in CO oxidation is constant in the size range of 4.0-14.0 nm Pd particles.[25] Phan et al. claimed that the Pd particle size (about 5-12 nm) does not affect the CO oxidation activity.[27] On the other hand, Peterson et al. reported that Pd dispersed atomically on Al_2O_3 is effective for CO oxidation activity than Pd nanoparticles at low temperature.[29] A microcalorimetric measurement and density functional calculations demonstrated that adsorption properties of CO on Pd nanoparticles consisting of <1000 atoms were considerably different than on Pd bulk.[33–36] Based on the above, the Pd particle size effect in a size region of 4 nm or less has not been clarified and the maximum activity for CO oxidation may be hidden in its size region.

Herein, we prepared Pd/Al_2O_3 catalysts with various particle sizes and alumina crystalline phases, and evaluated their CO oxidation activities. We expected that the control of particle size and strength of MSI will change shape and surface structures of metal nanoparticles. Combining X-ray absorption fine structure (XAFS), spherical aberration corrected scanning transmission electron microscopy (Cs-STEM) and infrared spectroscopy (IR) using CO as a molecular probe, we identified the size, shape and surface structure of Pd particle on Al_2O_3. Comparison between the relative fraction of various Pd surface site and the activities revealed the most active site for CO oxidation.

2. Experimental section

2.1. Catalyst preparation

γ-Al_2O_3 was obtained by thermal decomposition of boehmite (Sasol, PURAL alumina) at 500°C for 1 h. θ-Al_2O_3 (AKP-G07) was supplied from Sumitomo Chemical Co. Ltd. and calcined at 500°C for 1 h. Pd (Pd loading: 0.1–2wt%) were deposited onto alumina supports with various crystalline phases by the impregnation method using a 4.5wt% $Pd(NO_3)_2$ solution. The alumina supports were impregnated with an aquous 4.5wt% $Pd(NO_3)_2$ solution, and the suspension was stirred for 1 h. Excess water was removed by a rotary evaporator at 60°C, and then catalysts were dried at 80°C for 8 h and calcined at 300 or 500°C for 3 h. Some of the samples were further treated at 800, 850 or 900°C under air for 10 h to obtain Pd/Al_2O_3 catalysts with various Pd particles sizes.

Pd/ZSM-5 was prepared by ion exchange method. H-ZSM-5 was obtained by calcination of NH_4^+-ZSM-5 with Si/Al ratio of 20 (Tosoh Co., HSZ-840NHA) at 700°C for 30 min. 1.0 g of H-ZSM-5 stirred in 100 mL of an aqueous $Pd(NO_3)_2$ solution (containing 1.5 equivalent of Pd^{2+} based on Al content of H-ZSM-5) for 2 h at 45°C. The prepared sample was filtered and washed distilled water, dried at 80 °C over night, calcined at 500°C for 3 h. Pd loading of Pd/ZSM-5 was determined to be 0.26 wt% using inductively coupled plasma (ICP) analysis.

2.2. CO and H_2 pulse chemisorption

CO and H_2 pulse chemisorption measurement was performed using BEL-CAT-B (MicrotracBEL). An approximately 50-200 mg sample was put into a sample tube and pretreated under 100% O_2 at 300°C for 10 min and then under 100% H_2 at 300°C for 10 min. After the sample was cooled to 50°C in He, CO pulse chemisorption measurement was performed with 5% CO/He while monitoring the effluent with a thermal conductivity detector (TCD). In case of H_2

pulse chemisorption, the pretreated sample was exposed under Ar at 300 °C for 10 min to eliminate adsorbed H atoms on Pd and then cooled to 0°C, pulse chemisorption measurement was performed with 5% H_2/Ar. The dispersion of Pd was calculated from total adsorption gases by assuming that carbon monoxide and hydrogen were adsorbed on surface palladium at 1:1 (= Pd:CO) and 1:2 (= Pd:H_2) stoichiometry, respectively.

2.3. Aberration-corrected scanning transmission electron microscopy

The structure and size of Pd nanoparticles supported on Al_2O_3 were observed using JEM-ARM200F (JEOL Ltd.) Cs-corrected scanning transmission electron microscope operated at 200 kV. STEM images were recorded by a high angle annular dark field (HAADF) detector. Pd/Al_2O_3 catalysts were pretreated under a flowing mixture of 10% O_2/N_2 for 10 min and 10% H_2/N_2 for 10 min at 300°C. The samples were prepared by spreading a drop of methanol suspension of pretreated Pd/Al_2O_3 catalysts. The Pd particle size distribution was also estimated after CO oxidation. The samples of Figure S10 were prepared by oxidation in 10% O_2/N_2 at 300°C for 10 min and reduced in 10% H_2/N_2 at 300°C for 10 min, and then treated under 0.4% CO, 10% O_2, and N_2 balance at 130°C for 30 min.

2.4. Fourier transform infrared spectroscopy

FT-IR measurement was performed using a quartz in-situ IR cell and a JASCO FT/IR-6100 (JASCO Co.) with a liquid-nitrogen-cooled HgCdTe (MCT) detector. IR spectra were obtained by averaging 128 scans at a resolution of 4 cm^{-1}. The samples were pressed into approximately 50–100 mg of self-supporting disk and mounted into the IR cell with a CaF_2 window. The samples were pretreated by oxidation in 10% O_2/Ar at 300°C for 10 min and reduced in 10%

H_2/Ar at 300°C for 10 min. However, the samples used in previous work were oxidized at 400°C and reduced at 200°C. [15] The difference of pretreatment temperature did not almost affect oxidation state of Pd catalysts because PdO can be reduced to Pd metal below room temperature. After the samples were cooled to room temperature in Ar, IR spectra were taken as a background. CO (0.4% CO/Ar at a rate of 100 mL/min) was introduced into a quartz in-situ IR cell for 10 min. After physisorbed CO on Pd/Al_2O_3 catalysts was removed by a flowing of 100% Ar, IR spectra of adsorbed CO on Pd/Al_2O_3 were obtained.

2.5. X-ray absorption fine structure

Pd K-edge XAFS measurement was carried out on the BL14B2 beamline of the SPring-8 synchrotron radiation facility of the Japan Synchrotron Radiation Research Institute in Hyogo, Japan. The data analysis was performed using the Athena software including in the Demeter package. The samples were pretreated under 10% O_2/N_2 for 10 min at 300°C and then under 10% H_2/N_2 for 10 min at 300°C.

2.6. CO oxidation reaction

The CO oxidation was carried out using a conventional fixed-bed flow reactor at atmospheric pressure. Prior to performing an activity test, each sample (10 mg) inside a U-shaped quartz tube (inside diameter of 4 mm) was exposed to a flowing mixture of 10% O_2/N_2 for 10 min at 300°C and then 3% H_2/N_2 for 10 min at 300°C. The CO oxidation test was performed under 0.4% CO, 10% O_2, and N_2 balance at the total flow rate of 100 mL/min, corresponding to the gas hourly space velocity of 600,000 mL/g·h. The effluent gas was analyzed by a nondispersive infrared CO/CO_2 analyzer (Horiba VIA510). The CO conversion was obtained in steady-state from 100

to 200°C. The turnover frequency (TOF) was defined as the reaction rate per molar amount of surface Pd determined by CO pulse measurement. To compare the TOF between the catalysts at 130°C, the samples showing > 20 % CO conversion at 130°C were diluted with inert quartz to reduce CO conversion to < 20% to exclude thermal and gas diffusion problems. The TOF in Figure S6 was calculated using amount of surface Pd determined by H_2 pulse chemisorption.

3. Results

3.1. Catalyst preparation

Table 1 shows all Pd/Al_2O_3 catalysts examined in the present study. In Table 1, "Catalyst" is written as X nm Pd/Al_2O_3, and X corresponds to the average Pd particle size of Pd/Al_2O_3 estimated by CO pulse chemisorption. For the accuracy enhancement in the smaller Pd size region (< 9.0 nm), the catalyst preparation and the CO pulse chemisorption were performed for 1.5–9.0 nm Pd/γ-Al_2O_3 at least three times and average values for Pd dispersion and Pd particle size were displayed in Table 1. Based on the results of the repeated experiments, we renamed 1.9 nm Pd/γ-Al_2O_3 and 3.7 nm Pd/γ-Al_2O_3, 5.4 nm Pd/γ-Al_2O_3, and 7.7 nm Pd/γ-Al_2O_3 in ref. 31 to 2.6 nm Pd/γ-Al_2O_3 and 4.1 nm Pd/γ-Al_2O_3, 5.2 nm Pd/γ-Al_2O_3, 9.0 nm Pd/γ-Al_2O_3, respectively. In addition, particle size and dispersion calculated by H_2 pulse chemisorption were consistent with those estimated by CO pulse chemisorption excluding 0.1 wt% Pd/Al_2O_3 with high fraction of the isolated Pd atom (Table 1).

Table 1. Pd/Al_2O_3 catalysts used in this study as well as their Pd loadings, 1st and 2nd calcination temperature, dispersions, and average particle sizes.

Catalyst	Pd loading (wt%)	1st Calcination Temperature (°C)	2nd Calcination Temperature (°C)	CO pulse chemisorption		H_2 pulse chemisorption	
				Pd dispersion* (%)	Average Pd particle size* (nm)	Pd dispersion* (%)	Average Pd particle size* (nm)
1.5 nm Pd/γ-Al_2O_3	0.1	300	-	71±7	1.5±0.1	51	2.2
1.6 nm Pd/γ-Al_2O_3	0.2	300	-	71±1	1.6±0.1	60	1.9
2.2 nm Pd/γ-Al_2O_3	0.5	500	-	53.9±11	2.2±0.1	48	2.3
2.6 nm Pd/γ-Al_2O_3	1	500	-	45±9	2.6±0.5	38	2.9
4.1 nm Pd/γ-Al_2O_3	2	500	-	27±3	4.1±0.4	34	3.3
5.2 nm Pd/γ-Al_2O_3	2	500	800	24±9	5.2±1.1	21	5.3
9.0 nm Pd/γ-Al_2O_3	2	500	850	13±2	9.0±1.1	11	9.9
19 nm Pd/γ-Al_2O_3	2	500	900	6	19.1	7	15.9
1.2 nm Pd/θ-Al_2O_3	0.1	300	-	97	1.2	66	1.7
1.4 nm Pd/θ-Al_2O_3	0.2	300	-	83	1.4	77	1.5
1.5 nm Pd/θ-Al_2O_3	0.5	500	-	73	1.5	37	3
3.8 nm Pd/θ-Al_2O_3	1	500	-	29	3.8	25	4.5
5.4 nm Pd/θ-Al_2O_3	2	500	-	21	5.4	17	6.7
7.3 nm Pd/θ-Al_2O_3	2	500	800	15	7.3	13	8.5
14 nm Pd/θ-Al_2O_3	2	500	850	8	14.4	8	14.4
19 nm Pd/θ-Al_2O_3	2	500	900	6	19.2	6	18.1

*Calculated from Pd dispersion assuming spherical Pd particles.

3.2. XAFS measurement

XAFS measurement was performed to obtain information on the oxidation state and the coordination structure of Pd/Al_2O_3 catalysts. Figure 1a and 1b shows the Pd K-edge XANES spectra of Pd/Al_2O_3 and, Pd foil and PdO as reference samples. The XANES spectra of Pd/Al_2O_3 with smaller Pd particle were close to that of PdO reference. This indicates the presence of Pd^{2+} species in Pd/Al_2O_3 having Pd particle of 1–2 nm. As the particle size of

Pd/Al_2O_3 increased, the X-ray absorption intensity of Pd/Al_2O_3 at around 24,357 eV decreased. This trend was suggested that metallic Pd nanoparticles were formed on Al_2O_3 as the particle size increases.

The Fourier-transformed (FT) EXAFS spectra of $Pd/\gamma\text{-}Al_2O_3$ are displayed in Figure 1c. Pd-O scattering in PdO and Pd-Pd scattering in Pd foil were observed at the 1.6 and 2.5 Å, respectively. In 1.5 and 1.6 nm $Pd/\gamma\text{-}Al_2O_3$, only Pd-O scattering (at 1.6 Å) without Pd-Pd scattering (at around 2.5 Å) was observed, suggesting the presence of isolated Pd atom or amorphous-like Pd particles without periodic Pd-Pd bond. In contrast, Pd oxide particles were absent on Pd/Al_2O_3 because Pd oxide were reduced to Pd metal particle under H_2 flow at room temperature. The Pd-Pd scattering at 2.5 Å slightly appeared in 2.2 nm $Pd/\gamma\text{-}Al_2O_3$, and intensity of the Pd-Pd scattering peak increased as the particle size increased. On the other hand, the Pd-O scattering

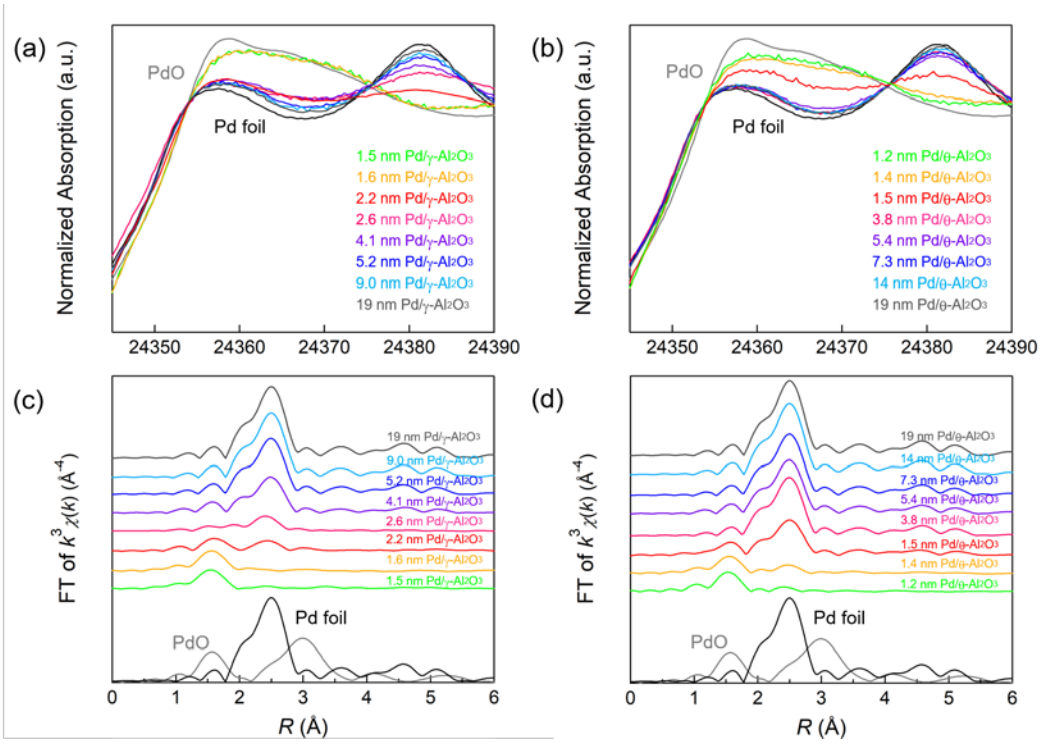

Figure 1. Pd K-edge (a, b) XANES and (c, d) FT-EXAFS spectra for Pd/Al_2O_3 with different average particle sizes after H_2 reduction, together with those of Pd foil (black line) and PdO (gray line) as references.

decreased and disappeared at 2.6 nm or more. These results mean that crystalline Pd metal particles were generated on Al_2O_3. Figure 1d shows the FT-EXAFS spectra of Pd/θ-Al_2O_3. However, a Pd-Pd scattering peak was clearly observed in the EXAFS spectrum of 1.5 nm Pd/θ-Al_2O_3 compared with 1–3 nm Pd/γ-Al_2O_3. The formation of crystalline Pd particles is preference on θ-Al_2O_3 than γ-Al_2O_3 because isolated Pd atom and amorphous Pd particles are more unstable on θ-Al_2O_3 weakly interacting with Pd.[9]

3.3. STEM images of Pd/Al_2O_3 catalysts

The Cs-STEM can visualize all Pd species (for example, single atoms and small clusters) on Al_2O_3 at atomic level. Figure 2 shows STEM images of three typical Pd/γ-Al_2O_3. The STEM images of other Pd/γ-Al_2O_3 are shown in Figure S1. The STEM or TEM images of 19 nm Pd/γ-Al_2O_3 and Pd/θ-Al_2O_3 with various Pd particle sizes are also displayed in ref. 31. A STEM image of 1.5 nm Pd/γ-Al_2O_3 displayed the presence of isolated Pd atoms and amorphous-like Pd particles which are smaller than 2 nm on γ-Al_2O_3 (Figure 2a). In 2.2 nm Pd/γ-Al_2O_3, amorphous-like Pd particles were mainly observed (Figure 2b). When the particle size increased to 5.3 nm, the Pd particle was in distorted shape and its surface was amorphous-like structure (Figure 2c). Even if the Pd particle size increased to 19 nm, the Pd particles maintained a distorted shape. The size distributions of Pd particles in Pd/γ-Al_2O_3 were obtained from STEM images (Table S1 and Figure S2). Pd particle in the size range of 0–0.3 nm denoted isolated Pd atom. The size distribution of 2.2 nm Pd/γ-Al_2O_3 exhibited a high fraction of the Pd nanoparticles smaller than 2.1 nm excluding isolated Pd atoms.

In 1.5 nm Pd/θ-Al_2O_3, isolated Pd atom and small amorphous Pd particles were observed. It was similar to the STEM image of 2.2 nm Pd/γ-Al_2O_3. However, the structural variation of Pd particles on θ-Al_2O_3 with weaker MSI was different from that on γ-Al_2O_3. The 7.3 nm Pd/θ-Al_2O_3 showed a spherical Pd particles. Growth of Pd particle to 19 nm caused transformation from spherical to well-faceted shape. In the size range of 4–19 nm, it was suggested that the fraction of thermodynamically stable facet such as Pd (111) increased as the Pd particle size increased.

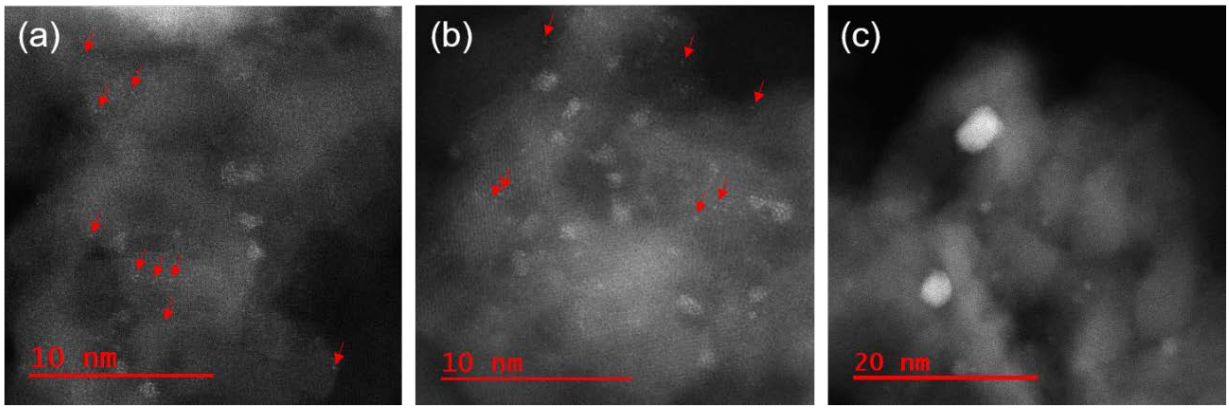

Figure 2. Typical STEM images of (a) 1.5 nm Pd/γ-Al_2O_3, (b) 2.2 nm Pd/Al_2O_3 and (c) 9.3 nm Pd/Al_2O_3. The red allows indicate the position of Pd single atom.

3.4. IR spectra of adsorbed CO

IR spectroscopy using CO as a molecular probe allows us to identify surface sites on metal nanoparticles because the wavenumber of the CO stretching vibration depend on a chemical state and a coordination number of the metal surface. Figure 3a shows two representative IR spectra of adsorbed CO on Pd/Al_2O_3. The intensities of IR bands were normalized because of difference of Pd loading and Pd dispersion. IR spectra of 1750–2300 cm^{-1} were well fitted with four stretching

vibration bands of CO adsorbed on Pd. The broad band centered at 2150 cm^{-1} is derived from linear adsorbed CO on cationic Pd species (Pd^{+}-CO_{linear}).[37–40] The band at around 2075 cm^{-1} is attributed to linear adsorbed CO on the corner of Pd particles or Pd(111) (Pd^{0}-CO_{linear}).[40–47] But, it is difficult to distinguish the corner sites and Pd(111) from the band of Pd^{0}-CO_{linear}. The band at 1980 cm^{-1} is attributed to bridge adsorbed CO on the step (Pd^{0}_{step}-CO_{bridge}).[33,42,44,45,47] The broad bands at 1750–1960 cm^{-1} are derived mainly from bridge or three–fold adsorbed CO on the plane including Pd(111) (Pd^{0}_{plane}-CO_{bridge}).[33,37–47] The band of linear and three-fold CO were observed, when CO is saturated adsorbed on Pd(111).[41]

Figure 3b and 3c (solid lines) shows the IR spectra of CO adsorbed on Pd/Al_2O_3 with various Pd particle sizes. Also, Figure 3b and 3c (dotted lines) shows the IR bands of each adsorbed CO species fitted by Gaussian function to quantify the Pd surface structure in the section 4.1. Figure 3b shows IR spectra of adsorbed CO on Pd/γ-Al_2O_3. In 1.5 nm Pd/γ-Al_2O_3, Pd^{+}-CO_{linear} and Pd^{0}-CO_{linear} bands were mainly observed. From the results of XAFS spectrum and TEM image of 1.5 nm Pd/γ-Al_2O_3, the cationic Pd species were identified isolated Pd atom on Al_2O_3. As the Pd particle size of Pd/γ-Al_2O_3 increased to 2.2 nm, the relative intensity of Pd^{+}-CO_{linear} band decreased and that of Pd^{0}-CO_{linear} and Pd^{0}_{plane}-CO_{bridge} band increased. This variation corresponds to a decrease of isolated Pd atom and generation of small Pd nanoparticles with amorphous structure. Thus, the amorphous-like Pd particles are considered to be the key structure for the formation of Pd corner sites. The Pd^{0}_{step}-CO_{bridge} band appeared when Pd particle size increased to 4 nm or more. Figure 3c shows the CO adsorption IR spectrum of Pd/θ-Al_2O_3. The IR spectra of adsorbed CO on Pd/θ-Al_2O_3 with Pd particles smaller than 2 nm was similar to that of 1–3 nm Pd/γ-Al_2O_3. However, with increasing the particle size from 1.5 nm to 7.3 nm, the relative intensity of Pd^{0}-CO_{linear} band decreased sharply and the Pd^{0}_{step}-CO_{bridge} band

appeared. This result meant that amorphous-like Pd particles grew to spherical Pd particle with high fraction of the step sites. Furthermore, as the particle size increased from 7.3 nm to 19 nm, the relative intensity of the Pd^0-CO_{linear} band increased due to transformation of Pd particles from

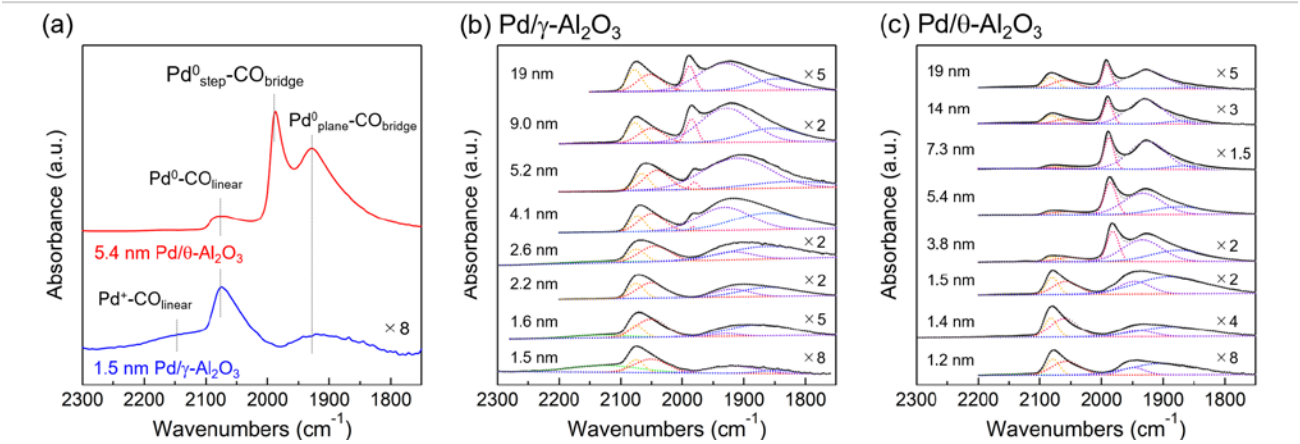

Figure 3. (a) IR spectra of CO chemisorbed to 1.5 nm Pd/γ-Al_2O_3 and 5.4 nm Pd/θ-Al_2O_3 at room temperature. The band centered at 2150 cm^{-1} is assigned to linear adsorbed CO on cationic Pd species (Pd^+-CO_{linear}). The band at around 2075 cm^{-1} is assigned to linear adsorbed CO on the corner of Pd particles or Pd(111) (Pd^0-CO_{linear}). The band at 1980 cm^{-1} is assigned to bridge adsorbed CO on the step (Pd^0_{step}-CO_{bridge}). The broad bands at 1750–1960 cm^{-1} are assigned mainly from bridge or three–fold adsorbed CO on the plane including Pd(111) (Pd^0_{plane}-CO_{bridge}). IR spectra of adsorbed CO at room temperature on (b) Pd/γ-Al_2O_3 and (c) Pd/θ-Al_2O_3 with various Pd particle sizes. IR spectra of 2.6–19 nm Pd/γ-Al_2O_3 and 1.5–19 nm Pd/θ-Al_2O_3 were previously reported in reference 31, Figure 2. Gaussian fittings of IR spectra were carried out for determination of the band areas at 2100-2200, 2000-2100, 1980, and 1750-1960 cm^{-1}.

spherical to well-faceted shape having such as a Pd(111).

3.5. CO oxidation activities of Pd/Al_2O_3 catalysts

Figures S3 and S4 show the CO conversion against reaction temperature using 10mg of Pd/Al_2O_3 catalysts with different particle sizes and alumina crystal phases. Since the Pd loading weight and dispersion are quite different between these Pd/Al_2O_3 catalysts, TOFs were calculated from <20% CO conversion where thermal and gas diffusion problems are negligible (Figure S5). Figure 4 shows the dependence of TOF of Pd/Al_2O_3 catalysts as a function of Pd particle size. As the particle size increased from 1.5 nm to 2.3 nm, the TOF of Pd/γ-Al_2O_3 increased from 0.07 s^{-1} to 0.20 s^{-1}, and the TOF reached a maximum value. When the particle size increased to 4 nm, the TOF sharply decreased to 0.07 s^{-1}. Then, the TOF gradually increased with increasing the particle size to 19 nm. The TOF of Pd/θ-Al_2O_3 also showed a similar trend of that of $Pd\gamma$-Al_2O_3. However, the TOF of Pd/θ-Al_2O_3 was less than a half of that of Pd/γ-

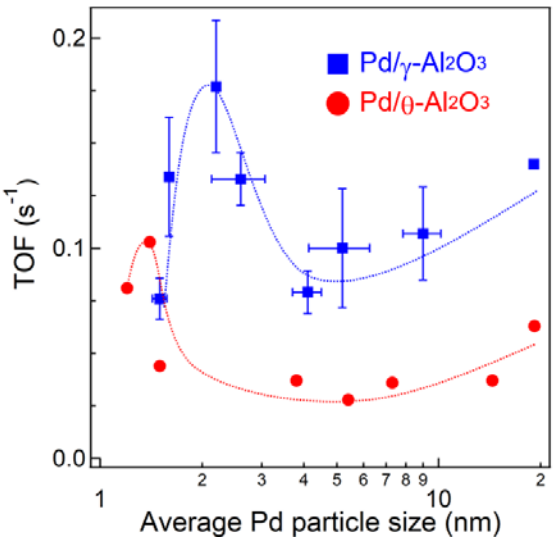

Figure 4. Dependence of TOFs at 130°C on average Pd particle size. Some error bars represent experimental error evaluated by repeating preparation of Pd/Al_2O_3, CO pulse measurement, and activity test at least three times.

Al_2O_3 in the size range of 4 nm or more. The increase of TOF in Pd/Al_2O_3 catalyst with particle size of 4–14 nm was slight and almost consistent with previous study reported by Haneda et al.[25] When TOFs were also calculated using Pd dispersion by H_2 chemisorption and plotted against Pd particle size (Figure S6), the trends were similar to Figure 4.

4. Discussions

4.1 Active Pd surface structure

To elucidate active sites for CO oxidation, the surface structure on Pd nanoparticles was quantified by IR spectra in Figure 3. The fraction of the Pd surface structure was determined from the band area of adsorbed CO species obtained by Gaussian fitting (Figure 3 and Table S2). Since the extinction coefficient of various adsorbed CO species is not clear, it should be noted that the fraction of the Pd surface structure is not an absolute value but a relative value. The fraction of Pd^0-CO_{linear} was plotted against Pd particle size in Figure 5a. The dependence of fraction of Pd^0-CO_{linear} on the particle size roughly agreed with that of TOF. The highest faction of the Pd^0-CO_{linear} was obtained in 2.2 nm Pd/γ-Al_2O_3, which showed the highest activity. In the size range of 8 nm or less, the high faction of the Pd^0-CO_{linear} was due to the presence of amorphous Pd particles with high fraction of corner sites. In contrast, in the size range of 8–19 nm, the increase of faction of the Pd^0-CO_{linear} derives from formation of Pd(111) on Pd particle. We estimated a particle size dependence of Pd site fraction on surface of Pd cubo-octahedron as a tentative model particle (Figure S7).[1,48] The particle size dependence of the fraction of Pd corner site + Pd(111) on the Pd particle model was similar to that determined from the IR spectra (Figure 5(a)). Therefore, the fraction of the Pd^0-CO_{linear} in the particle size of < 8 nm and > 8 nm in Figure 5(a) indicates the fraction of the corner and Pd(111), respectively. Comparing with

different crystalline alumina, γ-Al_2O_3 maintained a distorted structure of Pd nanoparticles with high fraction of corner sites due to stronger MSI. In contrast, Pd nanoparticles on θ-Al_2O_3 with weaker MSI formed high fraction of step sites. TOF was plotted against the fraction of Pd^0-CO_{linear} (Figure 5b). The trend between fraction of Pd^0-CO_{linear} and TOF showed a positive proportional relationship. Therefore, it was revealed that corner sites on Pd particles and Pd (111) are the highly active sites in CO oxidation. On the other hand, a positive relationship was not obtained between the fraction of Pd^+-CO_{linear}, $Pd^0{}_{step}$-CO_{bridge} or $Pd^0{}_{plane}$-CO_{bridge} and TOF

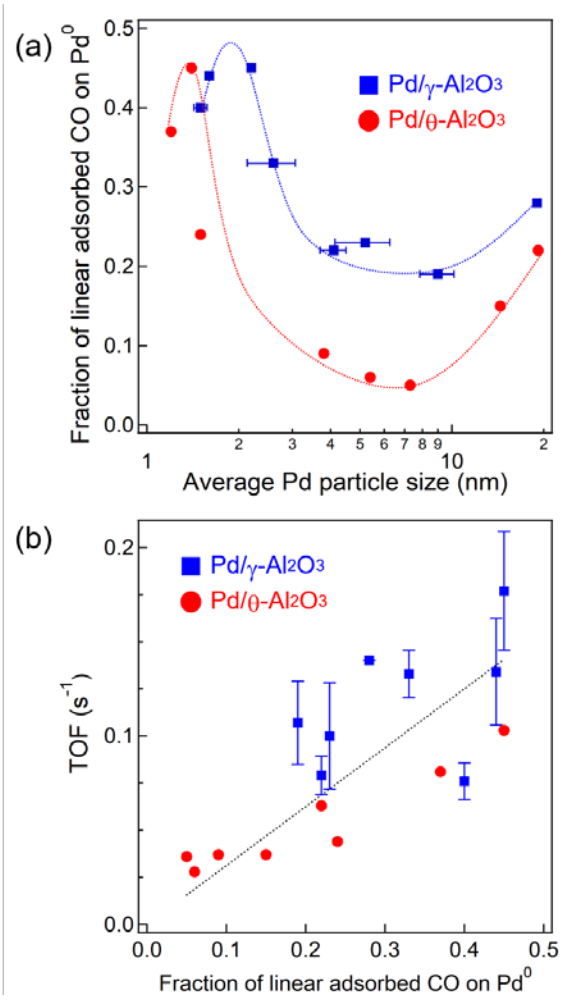

Figure 5. (a) Dependence of the fraction of linear adsorbed CO on Pd^0 on Pd particle size. (b) Plot of TOFs (at 130°C) against the fraction of linear adsorbed CO on Pd^0.

(Figure S8).

To investigate the reactivity of isolated Pd atom for CO oxidation, Pd/ZSM-5 catalyst (Pd loading: 0.26 wt%) was prepared by ion exchange method. An IR spectrum of adsorbed CO on Pd/ZSM-5 showed that Pd species on ZSM-5 were present as isolated Pd species (Figure S9a). CO conversion of Pd/ZSM-5 was lower than all Pd/Al_2O_3 catalysts at 130°C and TOF value of Pd/ZSM-5 was 0.009 s^{-1} (Figure S9b). Therefore, at 130°C, the isolated Pd atoms hardly contribute to the CO oxidation activity and Pd metal clusters/nanoparticles are more active than isolated Pd atoms.

4.2. Structure stability of Pd nanoparticle during CO oxidation

The stability of isolated Pd atoms and Pd nanoparticles on Al_2O_3 during CO oxidation was confirmed by STEM. The Pd particle size distribution of 2.2 nm Pd/γ-Al_2O_3 before or after CO oxidation at 130°C is shown in Figure S10. Since the size distribution hardly changed by the reaction, isolated Pd atoms and Pd nanoparticles were stable on Al_2O_3 under reaction conditions.

Avanesian et al. reported that surface reconstruction of Pt nanoparticle induced by CO adsorption at saturation coverage and >400 K.[18] Pt(100) facets on Pt nanoparticles were reconstructed into stepped surfaces with high concentrations of under-coordinated Pt atoms by the adsorption of CO. CO-induced reconstruction of Pd surface may occur during CO oxidation at 130°C. To confirm whether the surface of Pd nanoparticle was reconstructed by CO exposure, we observed adsorbed CO species on Pd/Al_2O_3 before and after CO oxidation (Figure S11). In comparison with Pd/Al_2O_3 before CO oxidation, IR spectra of Pd/Al_2O_3 after CO oxidation

showed that the band intensity of linear bound CO adsorbed on the corner sites decreased, while the band intensity of bridge bound CO adsorbed on the facets such as Pd(111) or Pd(100) increased. These results indicated that CO-induced reconstruction of Pd surface occur during CO oxidation at 130°C because bridge bound CO adsorbed on Pd facet is more thermodynamically stable than linearly bound CO adsorbed on Pd corner. The variation in the fraction of the linear adsorbed CO on Pd^0 was ~10%. The change of Pd surface structure was more largely influenced by Pd particle size and alumina crystalline phase than by CO-induced reconstruction. Figure S12 shows the plot of TOFs against the fraction of linear adsorbed CO on Pd^0 in Pd/Al_2O_3 after CO oxidation at 130°C. The order of fraction of Pd^0-CO_{linear} among Pd/Al_2O_3 catalysts treated under CO oxidation did not change. The trend between fraction of Pd^0-CO_{linear} in Pd/Al_2O_3 after CO oxidation and TOF also showed a positive proportional relationship. Thus, we considered that Pd corner sites and Pd(111) worked as dominant active sites during CO oxidation.

4.3. Mechanistic study

The kinetic analysis was carried out for Pd/Al_2O_3 with various Pd particle size. The apparent activation energies for CO oxidation of $Pd/\gamma\text{-}Al_2O_3$ with Pd particle size from 1.5~9.0 nm were 66-71 kJ mol^{-1} (Figure S13 and Table S3). Because there was little difference between their values, it was suggested that CO oxidation over all Pd/Al_2O_3 catalysts proceeded via the similar reaction mechanism. We investigated the dependence of CO and O_2 partial pressures on CO oxidation (Figure S14 and Table S3). Reaction orders with respect to CO and O_2 were negative value (-0.58~-0.89) and positive value (+0.66~+1.08), respectively. Therefore, it was suggested that CO oxidation on Pd metal surface proceeded in Langmuir-Hinshelwood mechanism, which is reaction of adsorbed CO and adsorbed O[49,50], or mechanism involved O_2 molecular adsorption and then adsorbed CO-assisted O_2 dissociation step[51]. It is difficult to determine that which mechanism is favor to proceed CO oxidation at low temperature over Pd particles. But, in either mechanism, self-poisoning of Pd metal surface by CO molecule inhibits dissociative adsorption or molecular adsorption of O_2. Thus, CO desorption from Pd surface at low temperature is the key for low temperature CO oxidation activity.[26]

From the above kinetic analysis, it was inferred that the desorption of CO from Pd surface is an important step for CO oxidation. Removal of CO from the Pd surface is necessary for subsequent activation of O_2. Thus, the desorption behavior of adsorbed CO from Pd/Al_2O_3 was observed by IR spectroscopy. CO was adsorbed on prereduced 4.1 nm $Pd/\gamma\text{-}Al_2O_3$ at 40°C and then the temperature of IR cell was risen to 120°C (at 10°C step) under Ar flow. In Figure 6a, the IR spectrum of 4.1 nm $Pd/\gamma\text{-}Al_2O_3$ at 40°C exhibited the three bands of $Pd^0\text{-}CO_{linear}$ (2000–2100 cm^{-1}), $Pd^0{}_{step}\text{-}CO_{bridge}$ (1960–2000 cm^{-1}), and $Pd^0{}_{plane}\text{-}CO_{bridge}$ (1750–1960 cm^{-1}), which was

similar to Figure 3b. When the temperature increased to 50–90°C, the three CO stretching vibration bands decreased. In particular, the decrease in the band intensity of Pd^0-CO_{linear} was remarkable, and the band of Pd^0-CO_{linear} disappeared completely when the temperature was

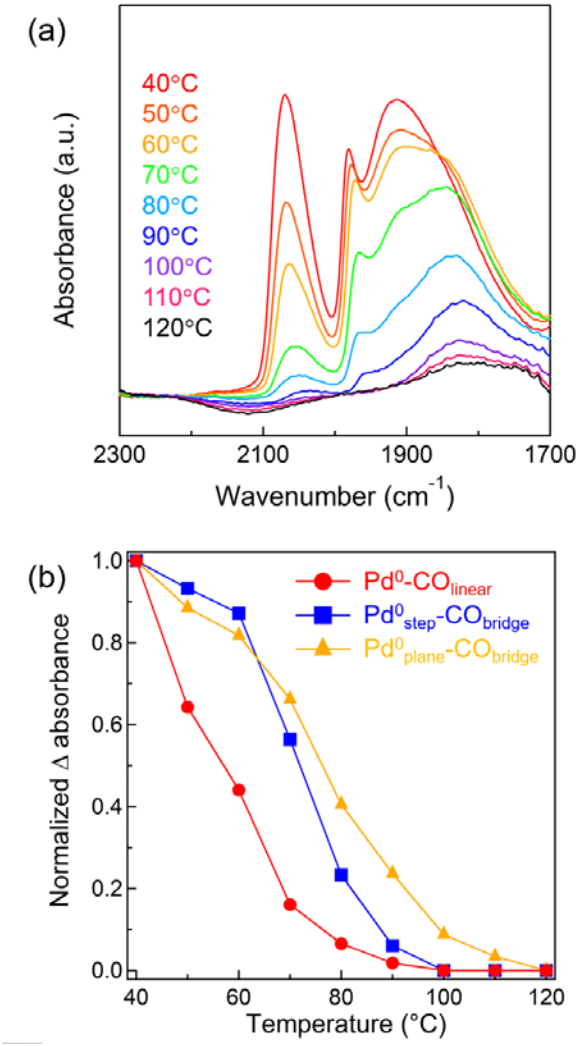

Figure 6. (a) FT-IR spectra of CO adsorbed on 4.1 nm Pd/γ-Al_2O_3 at various temperature under Ar. (b) Plot of normalized Δ absorbance against temperature. Normalized Δ absorbance calculated from the IR band intensity (●: Pd^0-CO_{linear} (at 2000–2100 cm^{-1}), ■: Pd^0_{step}-CO_{bridge} (at 1960–2000 cm^{-1}), ▲: Pd^0_{plane}-CO_{bridge} (at 1750–1960 cm^{-1})).

raised to 100°C.

To compare the adsorption strength of CO on different Pd surface sites, the decrease of absorbance of the CO adsorbed band on different surface sites was plotted against temperature (Figure 6b). Assuming that CO coverage of each surface site at 40 and 120°C is 100 and 0%, respectively, the CO coverage at various temperature (50–110°C) was evaluated from normalized Δ absorbance. A red shift of Pd^0_{plane}-CO_{bridge} band was due to decrease of CO coverage. When the temperature increased from 40 to 80°C, the normalized Δ absorbance of Pd^0-CO_{linear} more largely decreased than Pd^0_{step}-CO_{bridge} and Pd^0_{plane}-CO_{bridge}. At 100°C, the bridge bound CO adsorbed on Pd plane were only observed. Thus, the order in the adsorption strength of CO on the different Pd surface sites was Pd^0-CO_{linear} < Pd^0_{step}-CO_{bridge} < Pd^0_{plane}-CO_{bridge}. This order indicated that the linear adsorbed CO on Pd corner sites and Pd(111) easily desorbs than bridge adsorbed CO on Pd step and plane. Zeinalipour-Yazdi et al. reported that the order of CO adsorption energy follows linear < bridge < hollow-bound sites using DFT calculation.[52] To demonstrate linear adsorbed CO can easily desorb from Pd nanoparticles during CO oxidation, in-situ IR spectrum of adsorbed CO on Pd/Al_2O_3 during CO oxidation were obtained (Figure S15). The intensity of Pd^0-CO_{linear} band (at 2000–2100 cm^{-1}) was decreased to half of that as temperature increased from 50 to 110°C. In section 4.2, the fraction of Pd corner sites reconstructed to facet by adsorbed CO was ~0.05. Therefore, the decrease of Pd^0-CO_{linear} band was derived from not only CO-induced reconstruction but also formation of Pd vacancy site by CO desorption. In contrast, the intensities of Pd^0_{step}-CO_{bridge} (at 1960–2000 cm^{-1}) and Pd^0_{plane}-CO_{bridge} (at 1750–1960 cm^{-1}) band was slightly increased with increasing temperature due to CO-induced reconstruction. At 130°C, adsorbed CO on Pd particles was completely disappeared for reason that CO conversion reached almost 100%. The based on above in-situ IR study, at least a

part of Pd corner sites and Pd(111) were present as vacancy site to activate O_2 molecules during CO oxidation.

5. Conclusions

The Pd particle size effect on CO oxidation showed a complex tendency in the wide range of 1–19 nm. Concretely, as the Pd particle size increased from about 1 nm to 2 nm, the catalytic activity increased. But the activity sharply decreased with increasing particle size to 4 nm. Further growth of Pd nanoparticle to 19 nm, the activity slightly increased. In addition, Pd/γ-Al_2O_3 showed higher activity than Pd/θ-Al_2O_3 in the size range of 4–19 nm. These size effects were clearly understood using the fraction of Pd surface site obtained by IR spectra of adsorbed CO. The positive correlation between the fraction of Pd^0-CO_{linear} and the CO oxidation activity indicated that corners and Pd(111) on Pd particle are highly active sites. The fraction of Pd^0-CO_{linear} depended on the shape and surface structure of Pd particles supported on Al_2O_3. Approximately 2 nm Pd nanoparticles displayed amorphous structure with high fraction of the corner sites. On the other hand, growth to Pd particles to 19 nm promotes exposure of thermodynamically stable Pd(111). Comparing Pd/γ-Al_2O_3 and Pd/θ-Al_2O_3, distorted Pd particles on γ-Al_2O_3 have relatively higher fraction of highly active corner sites for CO oxidation than spherical or well-faceted Pd particles on θ-Al_2O_3. The structure sensitivity in CO oxidation over Pd nanoparticles was appeared by the CO adsorption strength depended on Pd surface site. The mechanistic study clarified that corner sites and Pd(111) promote CO oxidation due to the ease of CO desorption from the corner sites and Pd(111).

We previously reported step sites on Pd nanoparticles is highly active for CH_4 oxidation.[15] In contrast, corner sites and Pd(111) on Pd nanoparticles is effective for the activity of CO oxidation in this study. The active surface strongly depends on the reaction substrate. Therefore, to improve the catalytic activity of the supported metal nanoparticles, it is necessary to elucidate the shape and surface structure of the metal nanoparticles effective for the reaction substrate at an atomic scale.

ASSOCIATED CONTENT

Supporting Information.

Cs-STEM images of some Pd/γ-Al_2O_3; Counted particle number of Pd/γ-Al_2O_3 for size distribution; Size distributions for the number of Pd particles of various Pd/γ-Al_2O_3; CO conversion over Pd/γ-Al_2O_3; CO conversion over Pd/θ-Al_2O_3; CO conversion at 130°C on various amounts of 2.2 nm Pd/γ-Al_2O_3; Dependence of TOFs at 130°C on average Pd particle size estimated from H_2 pulse chemisorption; The ratios of the IR band area of various CO species on Pd/Al_2O_3; Particle size dependence of fraction of Pd surface site on particle size assuming a cubo-octahedron as a tentative model particle; Plot of TOFs against the fraction of various Pd surface site estimated from IR spectra; IR spectra of adsorbed CO on Pd/ZSM-5 and The CO conversion of Pd/ZSM-5 as a function of temperature.; Size distributions for the number of Pd particles of 2.2 nm Pd/γ-Al_2O_3 before and after CO oxidation; IR spectra of adsorbed CO on Pd/Al_2O_3 before and after CO oxidation.; Plot of TOFs against the fraction of linear adsorbed CO on Pd^0 for Pd/Al_2O_3 before and after CO oxidation.; The dependence of TOFs on

temperature for CO oxidation over Pd/γ-Al_2O_3; The dependence of TOFs on partial pressure of O_2 and CO for CO oxidation over Pd/γ-Al_2O_3; The apparent activation energy and the reaction order for CO oxidation over Pd/γ-Al_2O_3; IR spectra of adsorbed CO on 4.1 nm Pd/γ-Al_2O_3 measured under a flowing of reaction mixture at various temperature.

AUTHOR INFORMATION

Corresponding Author

*E-mail: satsuma@chembio.nagoya-u.ac.jp.

Notes

The authors declare no competing financial interest.

ACKNOWLEDGMENT

This work was partly supported by the JSPS KAKENHI Grant Grant-in-Aids and Challenging Exploratory Research (No.16K14476) from the Ministry of Education, Culture, Sports, Science and Technology (MEXT), Japan. A portion of this work was performed under management of the Elements Strategy Initiative for Catalysts & Batteries (ESICB), which is also supported by MEXT. XAFS measurement was carried out at BL14B2 of SPring-8 (Approval No. 2018B1756).

ABBREVIATIONS

XAFS, X-ray absorption fine structure; Cs-STEM, spherical aberration corrected scanning transmission electron microscopy; MSI, metal-support interaction; FT-IR, fourier transform infrared; HAADF, high angle annular dark field; TOF, turnover frequency; Pd^0-CO_{linear}, linear adsorbed CO on the corner of Pd particles or Pd(111); $Pd^0{}_{step}$-CO_{bridge}, bridge adsorbed CO on the step; $Pd^0{}_{plane}$-CO_{bridge}, bridge or three–fold adsorbed CO on the plane.

REFERENCES

(1) Hardeveld, R. V. A. N.; Hartog, F. THE STATISTICS OF SURFACE ATOMS AND SURFACE SITES ON METAL CRYSTALS. *Surf. Sci.* **1969**, *15*, 189–230.

(2) Bu, X. M.; Zhao, C. H.; Zhang, N.; Lin, S.; Gao, F.; Dai, X. W. Insights into the Reactivity of Supported Au Nanoparticles: Combining Theory and Experiments. *Top. Catal.* **2008**, *16*, 1074–1077.

(3) Williams, W. D.; Shekhar, M.; Lee, W. S.; Kispersky, V.; Delgass, W. N.; Ribeiro, F. H.; Kim, S. M.; Stach, E. A.; Miller, J. T.; Allard, L. F. Metallic Corner Atoms in Gold Clusters Supported on Rutile Are the Dominant Active Site during Water-Gas Shift Catalysis. *J. Am. Chem. Soc.* **2010**, *132*, 14018–14020.

(4) Shekhar, M.; Wang, J.; Lee, W.; Williams, W. D.; Kim, S. M.; Stach, E. A.; Miller, J. T.; Delgass, W. N.; Ribeiro, F. H. Size and Support Effects for the Water−Gas Shift Catalysis over Gold. *J. Am. Chem. Soc.* **2012**, *134*, 4700–4708.

(5) Ohyama, J.; Esaki, A.; Koketsu, T.; Yamamoto, Y.; Arai, S.; Satsuma, A. Atomic-Scale Insight into the Structural Effect of a Supported Au Catalyst Based on a Size-Distribution

Analysis Using Cs-STEM and Morphological Image-Processing. *J. Catal.* **2016**, *335*, 24–35.

(6) Cargnello, M.; Doan-Nguyen, V. V. T.; Gordon, T. R.; Diaz, R. E.; Stach, E. A.; Gorte, R. J.; Fornasiero, P.; Murray, C. B. Control of Metal Nanocrystal Size Reveals Metal-Support Interface Role for Ceria Catalysts. *Science* **2013**, *341*, 771–773.

(7) Carlsson, A.; Puig-Molina, A.; Janssens, T. V. W. New Method for Analysis of Nanoparticle Geometry in Supported Fee Metal Catalysts with Scanning Transmission Electron Microscopy. *J. Phys. Chem. B* **2006**, *110*, 5286–5293.

(8) Sanchez, S. I.; Small, M. W.; Bozin, E. S.; Wen, J. G.; Zuo, J. M.; Nuzzo, R. G. Metastability and Structural Polymorphism in Noble Metals: The Role of Composition and Metal Atom Coordination in Mono- and Bimetallic Nanoclusters. *ACS Nano* **2013**, *7*, 1542–1557.

(9) Li, L.; Wang, L. L.; Johnson, D. D.; Zhang, Z.; Sanchez, S. I.; Kang, J. H.; Nuzzo, R. G.; Wang, Q.; Frenkel, A. I.; Li, J.; et al. Noncrystalline-to-Crystalline Transformations in Pt Nanoparticles. *J. Am. Chem. Soc.* **2013**, *135*, 13062–13072.

(10) Kwak, J. H.; Hu, J.; Mei, D.; Yi, C.-W.; Kim, D. H.; Peden, C. H. F.; Allard, L. F.; Szanyi, J. Coordinatively Unsaturated Al^{3+} Centers as Binding Sites for Active Catalyst Phases of Platinum on γ-Al_2O_3. *Science* **2009**, *325*, 1670–1673.

(11) Ohyama, J.; Sato, T.; Yamamoto, Y.; Arai, S.; Satsuma, A. Size Specifically High Activity of Ru Nanoparticles for Hydrogen Oxidation Reaction in Alkaline Electrolyte. *J. Am. Chem. Soc.* **2013**, *135*, 8016–8021.

(12) Herzing, A. A.; Kiely, C. J.; Carley, A. F.; Landon, P.; Hutchings, G. J. Identification of Active Gold Nanoclusters on Iron Oxide Supports for CO Oxidation. *Science* **2008**, *321*, 1331–1335.

(13) Zhang, Z.; Zhu, Y.; Asakura, H.; Zhang, B.; Zhang, J.; Zhou, M.; Han, Y.; Tanaka, T.; Wang, A.; Zhang, T.; et al. Thermally Stable Single Atom Pt/m-Al_2O_3 for Selective Hydrogenation and CO Oxidation. *Nat. Commun.* **2017**, *8*, 16100.

(14) Mei, D.; Kwak, J. H.; Hu, J.; Cho, S. J.; Szanyi, J.; Allard, L. F.; Peden, C. H. F. Unique Role of Anchoring Penta-Coordinated Al^{3+} Sites in the Sintering of γ-Al_2O_3-Supported Pt Catalysts. *J. Phys. Chem. Lett.* **2010**, *1*, 2688–2691.

(15) Murata, K.; Mahara, Y.; Ohyama, J.; Yamamoto, Y.; Arai, S.; Satsuma, A. The Metal-Support Interaction Concerning the Particle Size Effect of Pd/Al_2O_3 on Methane Combustion. *Angew. Chemie Int. Ed.* **2017**, *56*, 15993–15997.

(16) Ding, K.; Gulec, A.; Johnson, A. M.; Schweitzer, N. M.; Stucky, G. D.; Marks, L. D.; Stair, P. C. Identification of Active Sites in CO Oxidation and Water-Gas Shift over Supported Pt Catalysts. *Science* **2015**, *350*, 189–192.

(17) Derita, L.; Dai, S.; Lopez-zepeda, K.; Pham, N.; Graham, G. W.; Pan, X.; Christopher, P. Catalyst Architecture for Stable Single Atom Dispersion Enables Site-Specific Spectroscopic and Reactivity Measurements of CO Adsorbed to Pt Atoms, Oxidized Pt Clusters, and Metallic Pt Clusters on TiO_2. *J. Am. Chem. Soc.* **2017**, *139*, 14150–14165.

(18) Avanesian, T.; Dai, S.; Kale, M. J.; Graham, G. W.; Pan, X.; Christopher, P. Quantitative and Atomic Scale View of CO-Induced Pt Nanoparticle Surface Reconstruction at

Saturation Coverage via DFT Calculations Coupled with in-Situ TEM and IR. *J. Am. Chem. Soc.* **2017**, *139*, 4551−4558.

(19) Kale, M. J.; Christopher, P. Utilizing Quantitative in Situ FTIR Spectroscopy to Identify Well-Coordinated Pt Atoms as the Active Site for CO Oxidation on Al_2O_3-Supported Pt Catalysts. *ACS Catal.* **2016**, *6*, 5599–5609.

(20) Qiao, B.; Wang, A.; Yang, X.; Allard, L. F.; Jiang, Z.; Cui, Y.; Liu, J.; Li, J.; Zhang, T. Single-Atom Catalysis of CO Oxidation Using Pt_1/FeOx. *Nat. Chem.* **2011**, *3*, 634–641.

(21) Hackett, S. F. J.; Brydson, R. M.; Gass, M. H.; Harvey, I.; Newman, A. D.; Wilson, K.; Lee, A. F. High-Activity, Single-Site Mesoporous Pd/Al_2O_3 Catalysts for Selective Aerobic Oxidation of Allylic Alcohols. *Angew. Chem. Int. Ed.* **2007**, *46*, 8593–8596.

(22) Kwon, Y.; Kim, T. Y.; Kwon, G.; Yi, J.; Lee, H. Selective Activation of Methane on Single-Atom Catalyst of Rhodium Dispersed on Zirconia for Direct Conversion. *J. Am. Chem. Soc.* **2017**, *139*, 17694–17699.

(23) Matsubu, J. C.; Yang, V. N.; Christopher, P. Isolated Metal Active Site Concentration and Stability Control Catalytic CO_2 Reduction Selectivity. *J. Am. Chem. Soc.* **2015**, *137*, 3076–3084.

(24) Tang, N.; Cong, Y.; Shang, Q.; Wu, C.; Xu, G.; Wang, X. Coordinatively Unsaturated Al^{3+} Sites Anchored Subnanometric Ruthenium Catalyst for Hydrogenation of Aromatics. *ACS Catal.* **2017**, 3–7.

(25) Haneda, M.; Todo, M.; Nakamura, Y.; Hattori, M. Effect of Pd Dispersion on the Catalytic Activity of Pd/Al_2O_3 for C_3H_6 and CO Oxidation. *Catal. Today* **2017**, *281*, 447–453.

(26) Satsuma, A.; Osaki, K.; Yanagihara, M.; Ohyama, J.; Shimizu, K. Activity Controlling Factors for Low-Temperature Oxidation of CO over Supported Pd Catalysts. *Appl. Catal. B Environ.* **2013**, *132–133*, 511–518.

(27) Phan, D. Q.; Kureti, S. CO Oxidation on Pd/Al_2O_3 Catalysts under Stoichiometric Conditions. *Top. Catal.* **2017**, *60*, 260–265.

(28) Ivanova, A. S.; Slavinskaya, E. M.; Gulyaev, R. V.; Zaikovskii, V. I.; Stonkus, O. A.; Danilova, I. G.; Plyasova, L. M.; Polukhina, I. A.; Boronin, A. I. Metal-Support Interactions in Pt/Al_2O_3 and Pd/Al_2O_3 Catalysts for CO Oxidation. *Appl. Catal. B Environ.* **2010**, *97*, 57–71.

(29) Peterson, E. J.; DeLaRiva, A. T.; Lin, S.; Johnson, R. S.; Guo, H.; Miller, J. T.; Hun Kwak, J.; Peden, C. H. F.; Kiefer, B.; Allard, L. F.; et al. Low-Temperature Carbon Monoxide Oxidation Catalysed by Regenerable Atomically Dispersed Palladium on Alumina. *Nat. Commun.* **2014**, *5*, 4885.

(30) Henry, C. R. Surface Studies of Supported Model Catalysts. *Surf. Sci. Rep.* **1998**, *31*, 231–325.

(31) Wang, Z.; Li, B.; Chen, M.; Weng, W.; Wan, H. Size and Support Effects for CO Oxidation on Supported Pd Catalysts. *Sci. China Chem.* **2010**, *53*, 2047–2056.

(32) Osaki, T. Effect of Sol–Gel Conditions on BET Surface Area, Pore Volume, Mean Pore Radius, Palladium Dispersion, Palladium Particle Size, and Catalytic CO Oxidation Activity of Pd/Al_2O_3 Cryogels. *J. Porous Mater.* **2012**, *11*, 697–711.

(33) Peter, M.; Florescamacho, J. M.; Adamovski, S.; Ono, L. K.; Dostert, K. H.; O'Brien, C. P.; Roldancuenya, B.; Schauermann, S.; Freund, H. J. Trends in the Binding Strength of Surface Species on Nanoparticles: How Does the Adsorption Energy Scale with the Particle Size? *Angew. Chem. Int. Ed.* **2013**, *52*, 5175–5179.

(34) Yudanov, I. V.; Metzner, M.; Genest, A.; Röseh, N. Size-Dependence of Adsorption Properties of Metal Nanoparticles: A Density Functional Study on Palladium Nanoclusters. *J. Phys. Chem. C* **2008**, *112*, 20269–20275.

(35) Lang, S. M.; Fleischer, I.; Bernhardt, T. M.; Barnett, R. N.; Landman, U. Low-Temperature CO Oxidation Catalyzed by Free Palladium Clusters: Similarities and Differences to Pd Surfaces and Supported Particles. *ACS Catal.* **2015**, *5*, 2275–2289.

(36) Fischer-Wolfarth, J. H.; Farmer, J. A.; Flores-Camacho, J. M.; Genest, A.; Yudanov, I. V.; Rösch, N.; Campbell, C. T.; Schauermann, S.; Freund, H. J. Particle-Size Dependent Heats of Adsorption of CO on Supported Pd Nanoparticles as Measured with a Single-Crystal Microcalorimeter. *Phys. Rev. B - Condens. Matter Mater. Phys.* **2010**, *81*, 8–11.

(37) Juszczyk, W.; Karpiński, Z.; Ratajczykowa, I.; Stanasiuk, Z.; Zieliński, J.; Sheu, L. L.; Sachtler, W. M. H. Characterization of Supported Palladium Catalysts III. Pd/Al_2O_3. *J. Catal.* **1989**, *120*, 68–77.

(38) Amalric-Popescu, D.; Bozon-Verduraz, F. SnO_2-Supported Palladium Catalysts : Activity in DeNOx at Low Temperature. *Catal. Lett.* **2000**, *64*, 125–128.

(39) Skotak, M.; Karpiński, Z.; Juszczyk, W.; Pielaszek, J.; Kępiński, L.; Kazachkin, D. V.; Kovalchuk, V. I.; D'Itri, J. L. Characterization and Catalytic Activity of Differently Pretreated Pd/Al_2O_3 Catalysts: The Role of Acid Sites and of Palladium-Alumina Interactions. *J. Catal.* **2004**, *227*, 11–25.

(40) Xu, J.; Ouyang, L.; Mao, W.; Yang, X.-J.; Xu, X.; Su, J.-J.; Zhuang, T.-Z.; Li, H.; Han, Y.-F. Operando and Kinetic Study of Low-Temperature, Lean-Burn Methane Combustion over a Pd/γ-Al_2O_3 Catalyst. *ACS Catal.* **2012**, *2*, 261–269.

(41) Szanyi, J.; Kuhn, W. K.; Goodman, D. W. CO Adsorption on Pd(111) and Pd(100): Low and High Pressure Correlations. *J. Vac. Sci. Technol. A Vacuum, Surfaces, Film.* **1993**, *11*, 1969.

(42) Wolter, K.; Seiferth, O.; Kuhlenbeck, H.; Bäumer, M.; Freund, H.-J. Infrared Spectroscopic Investigation of CO Adsorbed on Pd Aggregates Deposited on an Alumina Model Support. *Surf. Sci.* **1998**, *399*, 190–198.

(43) Ozensoy, E.; Meier, D. C.; Goodman, D. W. Polarization Modulation Infrared Reflection Absorption Spectroscopy at Elevated Pressures: CO Adsorption on Pd(111) at Atmospheric Pressures. *J. Phys. Chem. B* **2002**, *106*, 9367–9371.

(44) Tiznado, H.; Fuentes, S.; Zaera, F. Infrared Study of CO Adsorbed on $Pd/Al_2O_3{-}ZrO_2$. Effect of Zirconia Added by Impregnation. *Langmuir* **2004**, *20*, 10490–10497.

(45) Lear, T.; Marshall, R.; Lopez-Sanchez, J. A.; Jackson, S. D.; Klapötke, T. M.; Bäumer, M.; Rupprechter, G.; Freund, H. J.; Lennon, D. The Application of Infrared Spectroscopy to Probe the Surface Morphology of Alumina-Supported Palladium Catalysts. *J. Chem. Phys.* **2005**, *123*, 174706.

(46) Szanyi, J.; Kwak, J. H. Dissecting the Steps of CO_2 Reduction: 1. The Interaction of CO and CO_2 with γ-Al_2O_3: An in Situ FTIR Study. *Phys. Chem. Chem. Phys.* **2014**, *16*, 15117–15125.

(47) Ding, L.; Yi, H.; Zhang, W.; You, R.; Cao, T.; Yang, J.; Lu, J.; Huang, W. Activating Edge Sites on Pd Catalysts for Selective Hydrogenation of Acetylene via Selective Ga_2O_3 Decoration. *ACS Catal.* **2016**, *6*, 3700–3707.

(48) Ohyama, J.; Nishiyama, T.; Satsuma, A. Formation of Rhodium Metal Ensembles That Facilitate Nitric Oxide Reduction over Rhodium/Ceria in a Stoichiometric Nitric Oxide–Carbon Monoxide–Propene–Oxygen Reaction. *ChemCatChem* **2018**, *10*, 1651–1656.

(49) Engel, T.; Ertl, G. SURFACE RESIDENCE TIMES AND REACTION MECHANISM IN THE CATALYTIC OXIDATION OF CO ON Pd(111). *Chem. Phys. Lett.* **1978**, *54*, 95–98.

(50) Montemore, M. M.; Van Spronsen, M. A.; Madix, R. J.; Friend, C. M. O_2 Activation by Metal Surfaces: Implications for Bonding and Reactivity on Heterogeneous Catalysts. *Chem. Rev.* **2018**, *118*, 2816–2862.

(51) Allian, A. D.; Takanabe, K.; Fujdala, K. L.; Hao, X. X.; Truex, T. J.; Cai, J.; Buda, C.; Neurock, M.; Iglesia, E. Chemisorption of CO and Mechanism of CO Oxidation on Supported Platinum Nanoclusters. *J. Am. Chem. Soc.* **2011**, *133*, 4498–4517.

(52) Zeinalipour-Yazdi, C. D.; Willock, D. J.; Thomas, L.; Wilson, K.; Lee, A. F. CO Adsorption over Pd Nanoparticles: A General Framework for IR Simulations on Nanoparticles. *Surf. Sci.* **2016**, *646*, 210–220.

SYNOPSIS

Pd corner sites formed on small amorphous-like Pd particles and Pd (111) on large particles are highly active for CO oxidation than isolated Pd atoms and stepped surface like Pd(110).

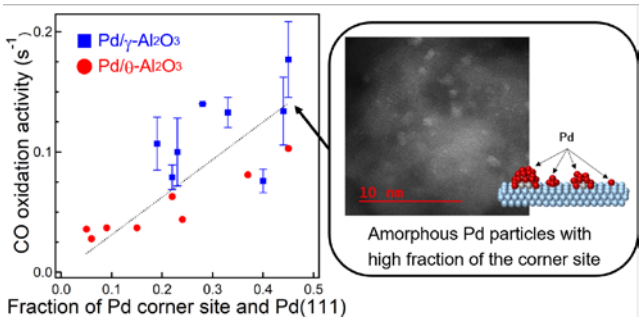

For Table of Contents Only